OPEN ACCESS
JOURNAL OF ADVANCED DIELECTRICS
Vol. 12, No. 3 (2022) 2250005 (13 pages)

DOI: 10.1142/S2010135X22500059

Experimental search for high-performance ferroelectric tunnel junctions guided by machine learning

Jingjing Rao[*,†], Zhen Fan[*,†,**], Qicheng Huang[*], Yongjian Luo[*], Xingmin Zhang[‡], Haizhong Guo[§], Xiaobing Yan[¶], Guo Tian[*], Deyang Chen[*], Zhipeng Hou[*], Minghui Qin[*], Min Zeng[*], Xubing Lu[*], Guofu Zhou[*,†], Xingsen Gao[*] and Jun-Ming Liu[‖]

[*]*Institute for Advanced Materials, South China Normal University, Guangzhou 510006, P. R. China*

[†]*Guangdong Provincial Key Laboratory of Optical Information Materials and Technology South China Normal University, Guangzhou 510006, P. R. China*

[‡]*Shanghai Institute of Applied Physics, Chinese Academy of Sciences, Shanghai 201204, P. R. China*

[§]*School of Physics and Microelectronics, Zhengzhou University, Zhengzhou 450001, P. R. China*

[¶]*Key Laboratory of Brain-Like Neuromorphic Devices and Systems of Hebei Province Hebei University, Baoding 071002, P. R. China*

[‖]*Laboratory of Solid State Microstructures and Innovation Center of Advanced, Nanjing 210093, P. R. China*

**fanzhen@m.scnu.edu.cn

Received 18 March 2022; Revised 20 April 2022; Accepted 28 April 2022; Published 15 June 2022

Ferroelectric tunnel junction (FTJ) has attracted considerable attention for its potential applications in nonvolatile memory and neuromorphic computing. However, the experimental exploration of FTJs with high ON/OFF ratios is a challenging task due to the vast search space comprising of ferroelectric and electrode materials, fabrication methods and conditions and so on. Here, machine learning (ML) is demonstrated to be an effective tool to guide the experimental search of FTJs with high ON/OFF ratios. A dataset consisting of 152 FTJ samples with nine features and one target attribute (i.e., ON/OFF ratio) is established for ML modeling. Among various ML models, the gradient boosting classification model achieves the highest prediction accuracy. Combining the feature importance analysis based on this model with the association rule mining, it is extracted that the utilizations of {graphene/graphite (Gra) (top), $LaNiO_3$ (LNO) (bottom)} and {Gra (top), $Ca_{0.96}Ce_{0.04}MnO_3$ (CCMO) (bottom)} electrode pairs are likely to result in high ON/OFF ratios in FTJs. Moreover, two previously unexplored FTJs: Gra/$BaTiO_3$ (BTO)/LNO and Gra/BTO/CCMO, are predicted to achieve ON/OFF ratios higher than 1000. Guided by the ML predictions, the Gra/BTO/LNO and Gra/BTO/CCMO FTJs are experimentally fabricated, which unsurprisingly exhibit ≥1000 ON/OFF ratios (~8540 and ~7890, respectively). This study demonstrates a new paradigm of developing high-performance FTJs by using ML.

Keywords: Machine learning; ferroelectric tunnel junctions; ON/OFF ratio; nonvolatile memory.

1. Introduction

Ferroelectric tunnel junction (FTJ) is an emerging memory device consisting of an ultra-thin ferroelectric layer sandwiched by two electrodes with different screening lengths. It relies on the polarization reversal to modulate the barrier height and/or width for the electron tunneling process, thereby showing ON and OFF states.[1,2] Owing to its high density, nondestructive readout, fast switching speed, low-power consumption, and analog switching capability,[3,4] FTJ has become a promising candidate device for next-generation nonvolatile memory and neuromorphic computing.[5,6]

The most important performance metric of an FTJ is perhaps the ON/OFF ratio, as it directly determines the read margin.[7] So far, a variety of approaches have been employed to improve the ON/OFF ratio, such as the integration with an semiconducting electrode,[8,9] interface engineering[10–12] and optimization of the ferroelectric layer thickness.[13,14] These enormous research efforts have led to a record ON/OFF ratio as high as 5.1×10^7.[15] However, most previous studies employed intuition- or trial-and-error-based experiments to optimize the device parameters of FTJs for high ON/OFF ratios. Moreover, only one or very few device parameters were optimized in these experiments due to the heavy workload. It is thus urgently needed to develop a general strategy considering all the device parameters (see Table 1) to guide the experiments in search of high-performance FTJs.

Machine learning (ML) offers an opportunity to develop such a general strategy. ML is a technique that uses algorithms to learn from the data and then apply the learned knowledge to make decisions/predictions.[25] In recent years, ML has been widely applied to accelerate the development of new materials and devices, such as high-temperature ferroelectrics,[26]

**Corresponding author.

Table 1. FTJ device parameters (features) influencing the ON/OFF ratio.

Device parameters	Which factor(s) influences the ON/OFF ratio	References
Substrate	Crystal orientation; Strain; Film quality…	16
Top electrode	Screening length; Ionic permittivity; Work function…	17
Ferroelectric material	Polarization; Static permittivity; Band structure…	18
Bottom electrode	Screening length; Ionic permittivity; Work function…	19
Thickness of ferroelectric layer	Barrier width…	20
Device area	Leakage current…	21
Preparation method	Film quality…	22
Oxygen pressure	Oxygen stoichiometry…	23
Temperature	Film quality…	24

lead-free piezoelectrics with large electrostrains,[27] high-performance organic photovoltaic materials,[28] and perovskite solar cells with high efficiencies.[29,30] These examples well demonstrate that ML is capable of establishing relationships between material/device descriptors and targeted performance and further predicting the performance of an unexplored material/device.

In this work, we develop an ML-based strategy to guide the experiments in search of high-performance FTJs. We first establish a dataset consisting of 152 FTJ data points collected from 106 papers published between 2009 and 2021. Each data point corresponds to one FTJ sample with its device parameters treated as the features and ON/OFF ratio treated as the target attribute. Then, multiple ML models are trained on this dataset, among which the gradient boosting classification model shows the highest prediction accuracy. Combining the feature importance analysis based on this model with the association rule mining, it is suggested that the utilizations of {graphene/graphite (Gra) (top), $LaNiO_3$ (LNO) (bottom)} and {Gra (top), $Ca_{0.96}Ce_{0.04}MnO_3$ (CCMO) (bottom)} electrode pairs are likely to result in high ON/OFF ratios in FTJs. Based on this, we further predict two unreported FTJs: Gra/$BaTiO_3$ (BTO)/LNO and Gra/BTO/CCMO, with ON/OFF ratios potentially higher than 1000. Experimentally, we fabricate the Gra/BTO/LNO and Gra/BTO/CCMO FTJs on the $SrTiO_3$ (STO) substrates and demonstrate that their ON/OFF ratios can reach ~8540 and ~7890, respectively, well consistent with our ML predictions. This work thus provides useful guidance for the development of high-performance FTJs.

2. Results and Discussion

We set up a standard workflow for the ML-guided development of high-performance FTJs, as shown in Fig. 1. It mainly consists of five steps: Dataset construction, ML model training, important feature extraction, prediction and experiments. Below are the detailed descriptions of the five steps and the corresponding results.

2.1. *Construction of FTJ dataset*

We first searched the papers related to FTJs via Google Scholar. As shown in Fig. 2(a), the number of papers related to FTJs increases from 452 in 2009 to 1960 in 2021, suggesting that FTJ is a research topic attracting increasing attention. However, only a small portion of these papers reported a complete set of the device parameters (Table 1) and ON/OFF ratios, which are called the source papers hereafter.

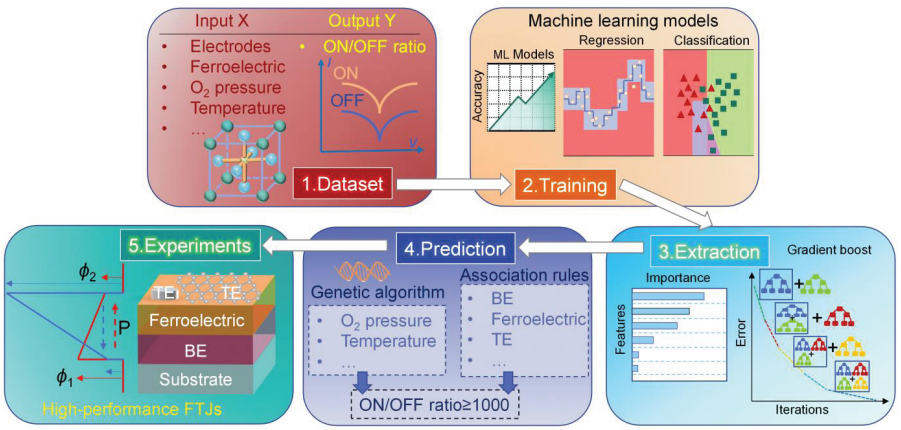

Fig. 1. Schematic illustration of the workflow for the ML-guided development of high-performance FTJs.

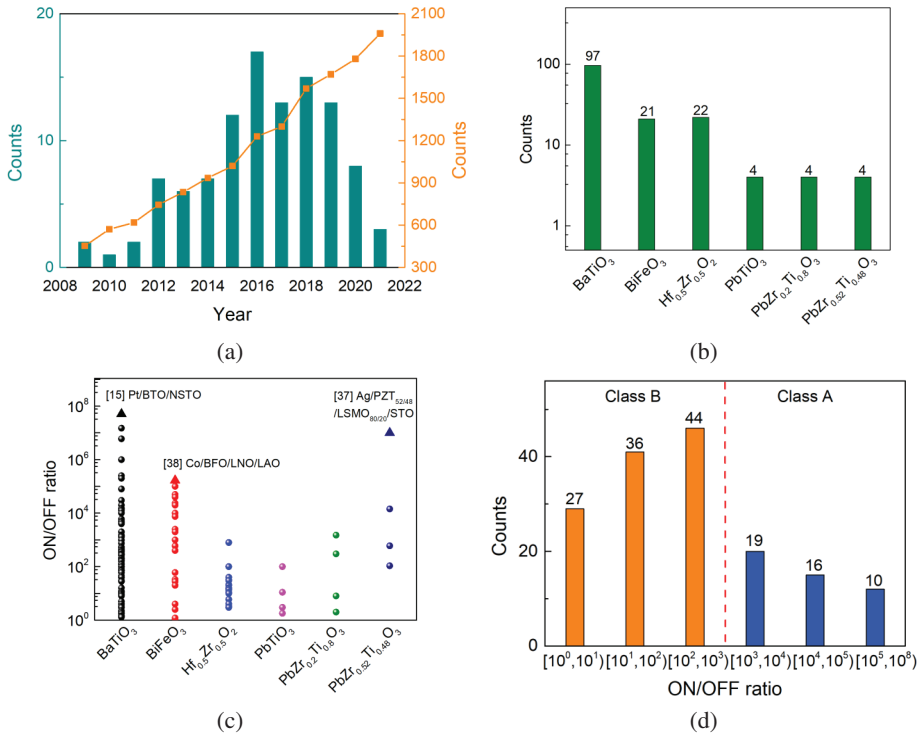

Fig. 2. (Color online) (a) Numbers of papers related to FTJs (orange line) and papers reporting the complete device parameters and ON/OFF ratios (cyan bar) as a function of year. (b) Frequencies of ferroelectric materials used in the 152 FTJ samples. (c) Distributions of ON/OFF ratios of FTJs based on different ferroelectric materials. The triangle symbols indicate the three FTJs with the highest ON/OFF ratios. (d) Numbers of FTJs in different ranges of ON/OFF ratios.

The evolution of the number of source papers with the year is presented in Fig. 2(a), revealing a total number of 106. From these 106 source papers, 152 FTJ samples were collected (see Table S1). Notably, all of these FTJ samples were based on oxide materials while those based on organic and two-dimensional materials were excluded due to the very limited number of those samples.

Figure 2(b) shows the ferroelectric materials used in the 152 FTJ samples and their frequencies that are used. The most used ferroelectric material is BTO, followed by $Hr_{0.5}Zr_{0.5}O_2$ (HZO) and $BiFeO_3$ (BFO). All these three materials exhibit persisted ferroelectric polarizations even in films with the thicknesses down to several nanometers.[31–33]

Besides, BTO possesses high-dielectric constant, low-dielectric loss, and high-breakdown field.[34] HZO is an emerging ferroelectric material compatible with standard CMOS processes.[35] BFO has a high Curie temperature and exhibits multiferroic behavior enabling the electric control of tunnel magnetoresistance.[36] The above outstanding features of BTO, HZO and BFO can explain why they are the three most used ferroelectric materials for FTJs.

Figure 2(c) shows the ON/OFF ratios of FTJs based on the different ferroelectric materials. The ON/OFF ratios are widely distributed, even for FTJs based on the same ferroelectric material. The thing of interest is how to fabricate an FTJ with a high ON/OFF ratio. We therefore focus on FTJs with the highest ON/OFF ratios in the respective BTO, PZT and BFO families, i.e., Pt/BTO/Nb: $SrTiO_3$ (NSTO),[15] Ag/$PbZr_{0.52}Ti_{0.48}O_3$ ($PZT_{52/48}$)/$La_{0.8}Sr_{0.2}MnO_3$ ($LSMO_{80/20}$)[37] and Co/BFO/LNO.[38] For the Pt/BTO/NSTO FTJ,[15] the low-oxygen-pressure fabrication was employed to introduce the oxygen vacancies. Consequently, both the oxygen vacancy migration and polarization switching could modulate the barrier height/width, leading to a giant ON/OFF ratio of 5.1×10^7. For the Ag/$PZT_{52/48}$/$LSMO_{80/20}$ FTJ,[37] due to the use of Ag top electrode (TE), the Ag ion migration was allowed and it synergized with the polarization switching, giving rise to an ON/OFF ratio as high as 10^7. The Co/BFO/LNO FTJ[38] was fabricated on the $LaAlO_3$ (LAO) substrate, which provided a high compressive strain to enhance the tetragonality and polarization of BFO. As a result, the ON/OFF ratio was improved to 1.67×10^5. The above strategies to achieve high ON/OFF ratios in FTJs focused on the optimization of only one device parameter, i.e., the oxygen pressure,[15] top electrode,[37] or substrate.[38] However, a general strategy considering all the device parameters (see Table 1) was still lacking.

We here used ML to develop such a general strategy. We constructed two datasets for ML regression and classification, respectively. Both datasets contain 152 FTJ samples and nine input features: Ferroelectric material, TE, bottom electrode (BE), substrate, device area, ferroelectric layer thickness, preparation method and oxygen pressure and temperature for film growth. In the dataset for regression, the ON/OFF ratio is

directly used as the output variable. By contrast, in the dataset for classification, the samples are divided into two classes: Class A and Class B with the ON/OFF ratios of ≥1000 and <1000, respectively. Class A (B) can be considered as the high-performance (low-performance) class, and the number of samples in it is 38 (114), as shown in Fig. 2(d). The label of the class is used as the output variable.

2.2. *ML modeling results*

We first attempted to directly predict the ON/OFF ratio of an FTJ based on its device parameters by using the ML regression. Seven typical regression models were employed, including gradient boosting, ridge, lasso, random forest, decision trees, extra trees, and *k*-nearest neighbors (KNN). These models were trained on a training set and assessed on a test set. The training and test sets were formed by randomly choosing 75% and 25% samples from the 152-sample dataset, respectively.

Figures 3(a) and 3(b) present the plots of actual versus predicted ON/OFF ratios for training and test, respectively, obtained from the gradient boosting regression model. It is clearly seen that the model fitness on the training set is much better than that on the test set. To quantify the model fitness, two indicators, i.e., root mean square error (RMSE) and coefficient of determination (R^2), were calculated. The RMSE values for training and test are 482000 and 2455000, respectively, while the corresponding R^2 values are 0.991 and

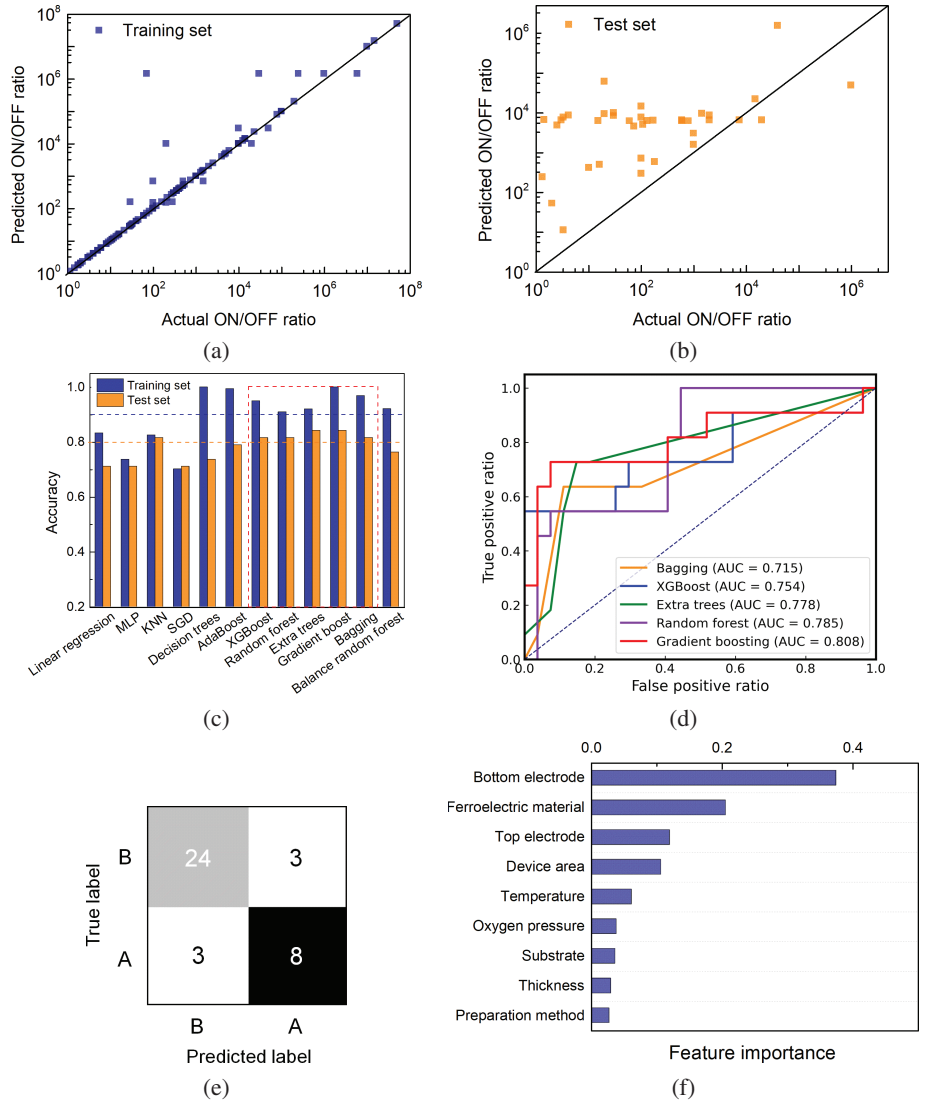

Fig. 3. (Color online) Actual versus predicted ON/OFF ratios for (a) training and (b) test computed by the gradient boosting regression model. (c) Accuracies of 12 classification models on training and test sets. The red dotted box indicates the five classification models which simultaneously achieve accuracies of >90% on the training set and accuracies of >80% on the test set. (d) ROC curves of the five classification models indicated by the red dotted box in c. (e) Confusion matrix and (f) feature importance ranking obtained from the gradient boosting classification model.

0.228, respectively. These results well indicate that the model fits the actual ON/OFF ratios very well on the training set but its predictive performance becomes much poorer on the test set, which is an issue called overfitting. This overfitting issue is ubiquitously observed in various regression models (see Table S2), suggesting that it may originate from the relatively small dataset size and is thus difficult to overcome. The ML regression is therefore not suitable to guide the experiments on FTJs. This motivates us to turn to the ML classification, which may exhibit better performance when the dataset size is small.

As described in Sec. 2.1, the FTJ samples with the ON/OFF ratios of ≥1000 and <1000 were classified into the high-performance class (Class A) and low-performance class (Class B). The goal of the ML classification was to correctly predict the class of an FTJ based on its device parameters. Twelve typical classification models were used, including linear regression, multi-layer perceptron (MLP), KNN, stochastic gradient descent (SGD), decision trees, extra trees, extreme gradient boosting (XGBoost), random forest, adaptive boosting (AdaBoost), gradient boosting, bagging and balance random forest. These models were trained and tested on the training and test sets, respectively (Note: The way to construct the training and test sets was similar to that used in the ML regression). Figure 3(c) shows the accuracies of the 12 models on the training and test sets. There are five models, i.e., XGBoost, random forest, extra trees, gradient boosting, and bagging, simultaneously achieving accuracies of >90% on the training set and accuracies of >80% on the test set. Among them, the gradient boosting model achieves the highest accuracy of 84.2% on the test set. Figure 3(d) further compares the receiver operating characteristic (ROC) curves and corresponding area under curve (AUC) values for the five models on the test set. A ROC curve is a plot of the true positive rate (TPR; the ratio of the number of samples which are correctly identified as Class A to that of truly high-performance samples) against the false positive rate (FPR; the ratio of the number of samples which are incorrectly identified as Class A to that of truly low-performance samples), and the closer an AUC value is to 1, the more accurately the samples are classified. It is seen from Fig. 3(d) that the gradient boosting model achieves the largest AUC value of 0.808. Because the gradient boosting model exhibits both the highest accuracy and largest AUC value on the test set, it is thus the model with the highest predictive power. Hereafter, we will focus mainly on the results obtained from the gradient boosting model (its hyperparameters are listed as follows: the learning rate is 0.6, the number of decision trees is 20, the fraction of samples randomly fed to each tree is 0.8, the maximum depth of the trees is 7 and the maximum number of features used for the node splitting is 9).

Figure 3(e) shows the confusion matrix[39] for the gradient boosting model on the test set. The gradient boosting model correctly classifies 8 out of 11 high-performance and 24 out of 27 low-performance FTJ samples into Class A and B, respectively. Interestingly, as seen in Table S3, most of the misclassified FTJ samples feature BTO and $La_{0.7}Sr_{0.3}MnO_3$ (LSMO) as the ferroelectric material and BE, respectively. This may be due to the large variations of the reported ON/OFF ratios in the BTO/LSMO-based FTJs.

2.3. *Important feature extraction*

Prior to using the gradient boosting model to predict FTJs which have not been reported so far, we performed the important feature extraction for dual purposes. First, one can develop some heuristics for the high performance of FTJs. In addition, by fixing the values of the identified important features to those leading to the high ON/OFF ratios, the search efficiency for high-performance FTJs can be improved. Figure 3(f) shows the feature importance ranking computed by the gradient boosting model. It is interesting to note that the BE, ferroelectric material and TE rank the top three most important features, which is quite consistent with the physical intuition. According to the well-established physical model of FTJ,[18,40,41] as shown in Fig. 4, the barrier height without the presence of polarization is determined by the band structures of the ferroelectric material and the electrodes. When the polarization is taken into account, the barrier height is modified by

$$\Delta\phi_i = e\frac{\gamma_i Q_s}{\varepsilon_0}, \quad i = 1,2, \tag{1}$$

$$\gamma_i = \frac{\delta_i}{\varepsilon_{M,i}}, \quad i = 1,2, \tag{2}$$

$$Q_s = \frac{Pd}{\varepsilon_F(\gamma_1+\gamma_2)+d}, \tag{3}$$

where $\Delta\phi_i$ is the magnitude of barrier height change at the interface between ferroelectric and M_i (M_1 and M_2 denotes the BE and TE, respectively), ε_0 is the permittivity of vacuum, e is the electron charge, Q_s is the screening charge density, δ_i and $\varepsilon_{M,i}$ are the screening length and ionic permittivity of electrode M_i while γ_i is its corresponding normalized screening length, P is the ferroelectric polarization, and d and ε_F are the thickness and static permittivity of the ferroelectric barrier, respectively.

The resistance change arises from the polarization switching-induced average barrier height change. More specifically, when there is no polarization, the barrier height at the interface between ferroelectric and M_i is ϕ_{i_0}, and the average barrier height is $\phi_0 = (\phi_{1\_0} + \phi_{2\_0})/2$. When the polarization is oriented upward (downward), ϕ_{1_0} is increased (decreased) by $\Delta\phi_1$ while ϕ_{2_0} is decreased (increased) by $\Delta\phi_2$, resulting in an average barrier height of ϕ_- (ϕ_+) (see Fig. 4). Thus, the average barrier height changes $\Delta\phi_{ave}$ upon polarization switching and consequent ON/OFF ratio are, respectively, given by

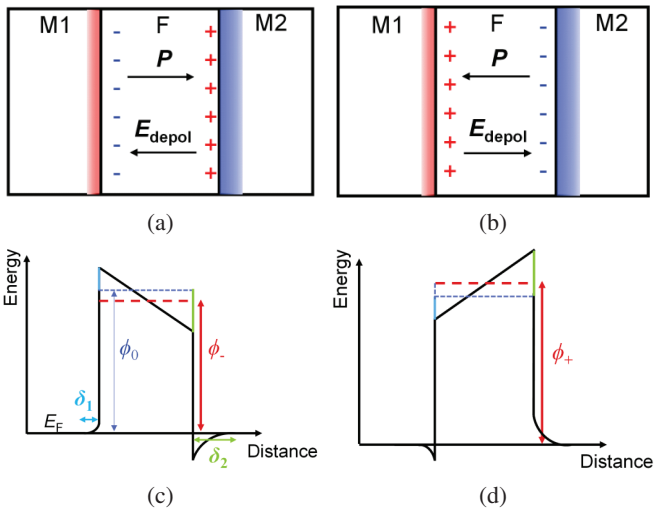

Fig. 4. (Color online) Schematics showing the (a, b) charge and electric field distributions and (c, d) potential energy profiles in an FTJ when the polarization of the ferroelectric (F) is oriented toward (a, c) TE (M_2) and (b, d) BE (M_1). In (a) and (b), the "+" and "–" signs indicate the positive and negative polarization charges, respectively, while the blue and red areas indicate the electrons and holes in the electrodes, respectively. In (c) and (d), ϕ_0 indicates the initial average barrier height, while ϕ_- and ϕ_+ indicate the average barrier heights for the polarization orientations shown in (a) and (b), respectively. δ_1 and δ_2 represent the screen lengths of the electrodes M_1 and M_2, respectively. E_F denotes the Fermi energy.

$$\Delta\phi_{ave} = \phi_+ - \phi_- = [\phi_0 + (\Delta\phi_2 - \Delta\phi_1)/2] - [\phi_0 + (\Delta\phi_1 - \Delta\phi_2)/2 = \Delta\phi_2 - \Delta\phi_1 = \frac{edP(\gamma_2 - \gamma_1)}{\varepsilon_0[\varepsilon_F(\gamma_2 + \gamma_1) + d]}, \quad (4)$$

$$\text{ON / OFF ratio} \approx \exp\left[\frac{\sqrt{2m}}{\hbar}\frac{|\Delta\phi_{ave}|}{\sqrt{\phi_0}}d\right] = \exp\left[\frac{1}{\hbar}\sqrt{\frac{2m}{\phi_0}}\frac{eP|\gamma_2 - \gamma_1|d^2}{\varepsilon_0[\varepsilon_F(\gamma_2 + \gamma_1) + d]}\right], \quad (5)$$

where m is the electron effective mass in the barrier, and $\hbar$ is the reduced Planck constant.

As can be seen from Eqs. (1)–(5), both the polarization of the ferroelectric material and the screening lengths of the electrodes can influence $\Delta\phi_{ave}$, thus affecting the ON/OFF ratio. Therefore, the BE, ferroelectric material and TE are the three most important factors influencing the ON/OFF ratio.

Then, we proceeded to investigate what values of the important features can result in high ON/OFF ratios for FTJs by using the association rule mining. One-factor associations were implemented, and three parameters: *support*, *confidence* and *lift* were calculated to evaluate the association rules. These three parameters can be explained through the following example.

Table 2. Association rule mining for FTJs with ON/OFF ratios of ≥1000 (i.e., Class A).

Consequent This feature is used in Class A.	Support This is a fraction of all data belonging to Class A and has feature listed in the first column.	Confidence This is a fraction of data in Class A has feature listed in the first column.	Lift This is a ratio between the confidence and the fraction of data in dataset has feature listed in the first column.
Substrate:			
STO	0.211	0.711	1.08
$YAlO_3$ (YAO)	0.053	0.018	2.702
LAO	0.007	0.022	3.378
TE:			
Co	0.072	0.244	1.77
LSMO	0.013	0.044	0.751
Gra	0.013	0.044	1.689
Pt	0.132	0.444	1.056
Ag	0.013	0.044	0.751
Au	0.013	0.044	0.676
BE:			
LSMO	0.053	0.178	0.772
CCMO	0.053	0.178	2.702
LNO	0.013	0.044	2.252
$SrRuO_3$ (SRO)	0.013	0.044	0.356
Ferroelectric:			
$PbZr_{0.2}Ti_{0.8}O_3$ ($PZT_{20/80}$)	0.007	0.022	0.844
BFO	0.072	0.244	1.77
BTO	0.204	0.689	1.08

As shown in Fig. 2(d), among the 152 total FTJ samples, there are 45 samples with the ON/OFF ratios of ≥1000 (Class A). In Class A, 31 samples are based on BTO. Therefore, the fraction of samples which are in Class A and simultaneously based on BTO in the whole dataset is 31/152, leading to a *support* of 0.204 (see Table 2). The fraction of such samples in the Class A is 31/45, leading to a *confidence* of 0.689. The values of *support* and *confidence* seem to be high. However, based on only these two parameters one could not conclude the validity of the rule that using BTO as the ferroelectric material in an FTJ is likely to result in a high ON/OFF ratio (≥1000). Instead, the high *support* and *confidence* values may be simply due to the large number of the BTO-based samples. To find a more suitable evaluation criterion, the lift is therefore resorted to. The *lift* value for BTO is calculated as the confidence divided by the fraction of BTO-based samples, i.e., 0.689/(97/152) = 1.08, quite close to 1. This suggests that BTO has almost no relationship with a high ON/OFF ratio. If the *lift* for certain feature value is higher (lower) than 1, there may be a positive (negative) correlation between that feature value and the high ON/OFF ratio. For example, the *lift* for BFO (PZT) is higher (lower) than 1, suggesting that BFO (PZT) is likely to result in a high (low) ON/OFF ratio (see Table 2).

In terms of the BE, the *lift* values for CCMO and LNO are higher than 1 (2.702 and 2.252, respectively; see Table 2), suggesting that they are beneficial to high ON/OFF ratios. This is physically reasonable because both LNO and CCMO have relatively large screening lengths, i.e., ~0.6 nm[42] and ~1.8 nm,[43] respectively, which can enhance the ON/OFF ratio based on Eqs. (1)–(5).

Turning to the TE, Co and Gra exhibit *lift* values higher than 1, which are 1.77 and 1.689, respectively. For the Co TE, it not only provides a relatively large screening length (~1.5 Å),[44] but also induces charge trapping effect at the Co/ferroelectric interface,[45] both of which contribute to a high ON/OFF ratio. However, because the charge trapping is an extrinsic effect, the Co TE will not be further considered hereafter. For the Gra TE, the low density of states near its Dirac point and the small quantum capacitance can result in a large Fermi level shift upon polarization switching, thus enhancing the ON/OFF ratio.[46,47]

The above results suggest that using electrode pairs of {Gra, CCMO} and {Gra, LNO} may be a useful strategy to obtain high ON/OFF ratios for FTJs. Using the ferroelectric material of BFO may also be useful, but this strategy limits the choice of the ferroelectric material. In order to facilitate the development of high-performance of FTJs based on various emerging ferroelectric materials, we focus on the strategy of using electrode pairs of {Gra, CCMO} and {Gra, LNO}. New high-performance FTJs based on these electrode pairs will be predicted as follows.

2.4. *Prediction*

The prediction was performed with the gradient boosting model. The electrode pairs were fixed to be {Gra, CCMO} and {Gra, LNO}, because they were likely to result in high ON/OFF ratio, as identified in Sec. 2.3. In order to highlight the roles of Gra, CCMO and LNO, LSMO and Pt having *lift* values close to (or lower than) 1 were used as the control BE and TE, respectively. The ferroelectric material and substrate were purposely chosen to be BTO and STO, respectively, because they have little influence on the ON/OFF ratio as suggested by their *lift* values being close to 1 (see Table 2). Other feature values were searched and optimized by using the genetic algorithm.

Table 3 lists the performances of six FTJs predicted by the gradient boosting model. The Gra/BTO/LNO and Gra/BTO/CCMO FTJs are the two samples designed following the strategy of using electrode pairs of {Gra, LNO} and {Gra, CCMO}. While the other four FTJs are the control samples. The predicted results show that the Gra/BTO/LNO and Gra/BTO/CCMO FTJs exhibit the ON/OFF ratios of ≥1000 while the control FTJs all exhibit the ON/OFF ratios of <1000. This indicates that that the electrode pairs {Gra, LNO} and {Gra, CCMO} are beneficial to obtaining high ON/OFF ratios, consistent with the above results of association rule mining (see Sec. 2.3). It is also noteworthy that the Gra/BTO/LNO and Gra/BTO/CCMO FTJs have never been reported previously.

Table 3. Six FTJs predicted by the gradient boosting model, among which the Gra/BTO/LNO and Gra/BTO/CCMO FTJs are the two samples designed following the strategy of using electrode pairs of {Gra, LNO} and {Gra, CCMO}, while the other four FTJs are the control samples.

No.	Substrate	Top electrode	Ferroelectric material	Bottom electrode	Preparation method	Oxygen pressure (Pa)	Temperature (°C)	Thickness (nm)	Device area (μm^2)	Is the ON/OFF ratio predicted to be ≥1000?
1	STO	Gra	BTO	LNO	PLD	~1	~700	4.8	~7850	Yes
2	STO	Gra	BTO	CCMO	PLD	~1	~700	4.8	~7850	Yes
3	STO	Pt	BTO	LNO	PLD	~1	~700	4.8	~200	No
4	STO	Pt	BTO	CCMO	PLD	~1	~700	4.8	~200	No
5	STO	Pt	BTO	LSMO	PLD	~1	~700	4.8	~200	No
6	STO	Gra	BTO	LSMO	PLD	~1	~700	4.8	~2000	No

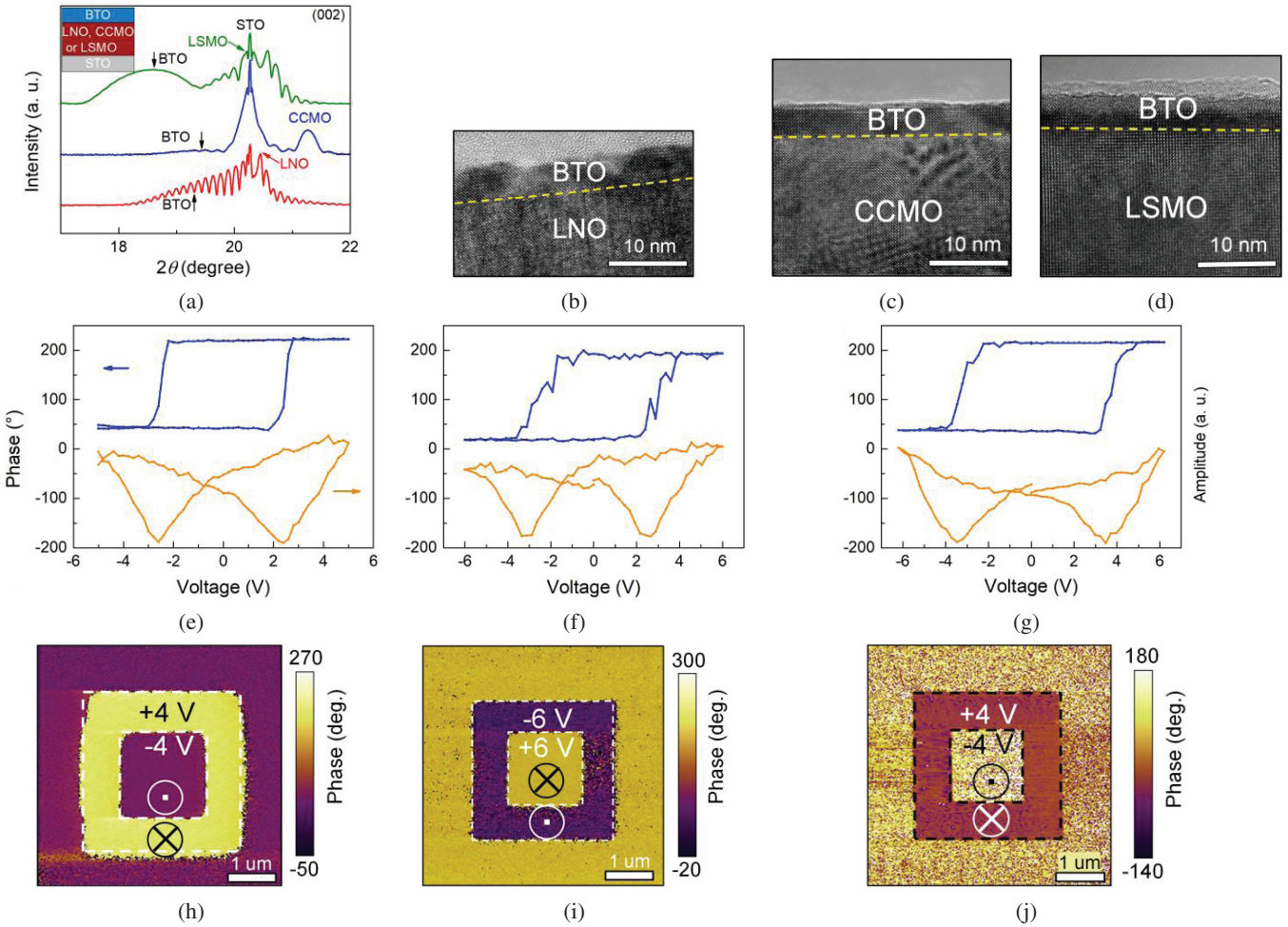

Fig. 5. (a) Synchrotron θ-2θ XRD (002) patterns of BTO/LNO, BTO/CCMO, BTO/LNO samples. Inset shows the stacking of different layers. Cross-sectional STEM images of (b) BTO/LNO, (c) BTO/CCMO and (d) BTO/LNO samples. Local PFM phase (top) and amplitude (bottom) loops measured on the bare BTO films with (e) LNO, (f) CCMO and (g) LSMO bottom electrodes. PFM out-of-plane phase images recorded after writing different box-in-box areas in (h) BTO/LNO, (i) BTO/CCMO and (j) BTO/LSMO films using +4 V/−4 V, −6 V/+6 V and +4 V/−4 V, respectively.

In order to confirm their high performances, the Gra/BTO/LNO and Gra/BTO/CCMO FTJs as well as the control samples (Pt/BTO/LNO, Pt/BTO/CCMO, Pt/BTO/LSMO, and Gra/BTO/LSMO) were experimentally fabricated following the predicted feature values shown in Table 3. The next section will present the experimental results.

2.5. *Experiments*

Guided by the ML prediction, ~4.8 nm-thick BTO films were epitaxially grown on the STO substrates with three different BE layers: LNO, CCMO and LSMO. All the BTO/LNO, BTO/CCMO, and BTO/LSMO samples exhibit smooth surfaces (see Fig. S1). Figure 5(a) shows the synchrotron X-ray diffraction (XRD) (002) scans of these three samples. Sharp (002) peaks along with fringes from the LNO, CCMO and LSMO layers are observed, demonstrating their good epitaxy qualities on the STO substrates. However, the BTO layers in the three samples exhibit (002) peaks with different positions and intensities, suggesting different strain states and epitaxy qualities. The out-of-plane lattice parameters of BTO (c_{BTO}) are calculated to be 4.099 Å, 4.070 Å and 4.249 Å, for the BTO/LNO, BTO/CCMO, and BTO/LSMO samples, respectively.

To further reveal the BTO structures in the three samples, scanning transmission electron microscopy (STEM) was performed. Figures 5(b)–5(d) show that the BTO layers in all the samples exhibit tetragonal structures, but the out-of-plane and in-plane lattice parameters (c_{BTO} and a_{BTO}, respectively) are different. In the BTO/LNO sample (Fig. 5(b)), c_{BTO} is observed to be 4.125 Å, consistent with the XRD result, while a_{BTO} is observed to be 3.935 Å. This a_{BTO} value is smaller than that of bulk BTO (~3.992 Å),[48] suggesting that BTO is subjected to a 1.43% compressive strain. This compressive strain is provided by the LNO layer exhibiting an a_{LNO} of 3.981 *Å*, and it in turn leads to the slight elongation of c_{BTO}.

In the BTO/CCMO sample (Fig. 5(c)), c_{BTO} and a_{BTO} are observed to be 4.088 Å and 3.966 Å, respectively, while a_{CCMO} is only 3.730 Å. The large difference between a_{BTO} and a_{CCMO} suggests that the strain is almost fully relaxed, leading to a relatively short c_{BTO}. In addition, incoherent interfaces between BTO and CCMO and dislocation-like defects in the BTO layer are observed (Fig. 5(c)), contributing to the strain relaxation. These defects also cause low BTO peak intensity in the XRD pattern, as shown in Fig. 5(a).

In the BTO/LSMO layer (Fig. 5(d)), c_{BTO} and a_{BTO} are observed to be 4.233 Å and 3.925 Å, respectively, indicating that BTO is subjected to a quite large compressive strain of 1.68%. Such large compressive strain is attributed to the small a_{LSMO} (3.941 Å) and the coherent interface between BTO and LSMO.

The above XRD and TEM results confirm that epitaxial BTO films with the same tetragonal phase but different lattice parameters are successfully grown on the STO substrates with three different BE layers: LNO, CCMO and LSMO.

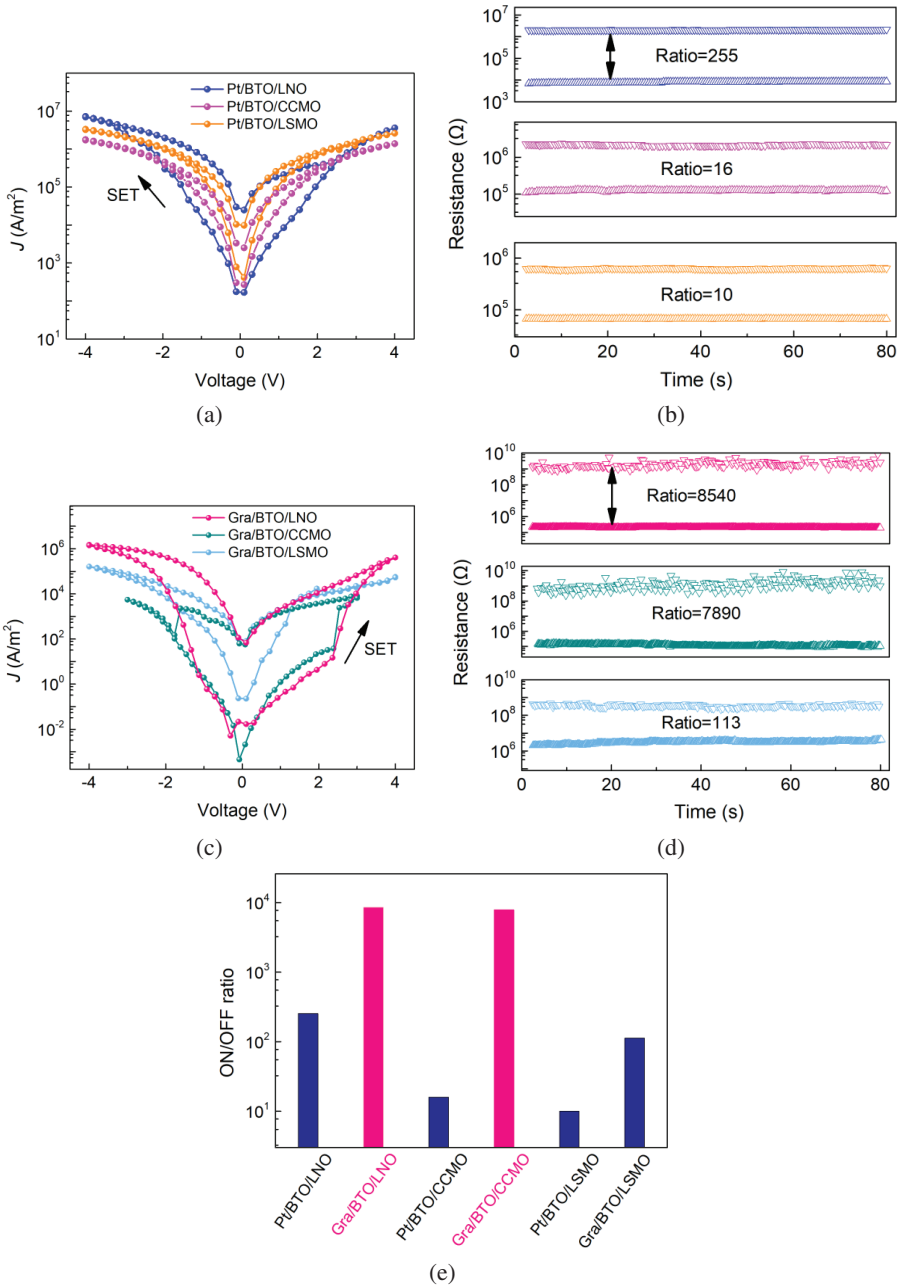

Fig. 6. (a) *J-V* characteristics and (b) retention behaviors (read at 0.3 V) of the Pt/BTO/LNO, Pt/BTO/CCMO and Pt/BTO/LSMO devices. (c) *J-V* characteristics and (d) retention behaviors (read at 0.3 V) of the Gra/BTO/LNO, Gra/BTO/CCMO and Gra/BTO/LSMO devices. In (b) and (d), symbols of upward and downward triangles indicate the LRS and HRS, respectively. (e) Summary of the ON/OFF ratios of six FTJs.

To characterize the ferroelectric properties[49] of the BTO films, piezoresponse force microscopy (PFM) was performed. The voltages were applied to conductive Pt tips in contact with the bare films, while the bottom electrodes were grounded. Figures 5(e)–5(g) show the PFM amplitude and phase hysteresis loops of the BTO films on the LNO, CCMO and LSMO bottom electrodes, respectively. All the amplitude loops exhibit a butterfly shape and the phase loops exhibit sharp ~180° switching, demonstrating the occurrences of ferroelectric polarization switching in the BTO films.

The ferroelectricity was further investigated via the PFM imaging. Box-in-box areas in the BTO/LNO, BTO/CCMO and BTO/LSMO films were scanned with tip biases of +4 V/−4 V, −6 V/+6 V and +4 V/−4 V, respectively. Figures 5(h)–5(j) show the sharp phase contrasts between the areas written with positive and negative tip biases, indicating that the ferroelectric domains in the two areas are oriented to the downward and upward directions, respectively. In addition, Figs. 5(h) –5(j) also show that the as-grown BTO/LNO and BTO/LSMO films are self-polarized with polarization pointing upward, while the as-grown BTO/CCMO is self-polarized with polarization pointing downward. The different self-polarization orientations may arise from different strain gradients,[50,51] interfacial built-in fields[52,53] and screening charges[54] in these samples.

Besides the PFM studies conducted on the bare BTO films (Pt tips acting as the TE), the PFM hysteresis loops were also measured on the Gra-electroded BTO films (see Fig. S2). Both butterfly-shaped amplitude loops and square phase loops showing ~180° switching are observed in the Gra/BTO/LNO, Gra/BTO/CCMO, and Gra/BTO/LSMO devices, confirming that the polarization of BTO can be switched in all these devices.

Six FTJ devices were constructed by depositing Pt TE and exfoliating Gra TE on the BTO/LNO, BTO/CCMO and BTO/LSMO films. The current density–voltage (*J*-*V*) loops of these devices were measured using the dc voltage sweep mode. The voltages were applied to the TEs while the bottom electrodes were grounded. Figure 6(a) shows the *J*-*V* loops of Pt/BTO/LNO, Pt/BTO/CCMO and Pt/BTO/LSMO devices in semi-logarithmic scale. All the devices exhibit bipolar resistive switching behavior with the SET transition occurring in the negative voltage regime, and their high and low resistance states (HRS and LRS, respectively) are observed to be stable (Fig. 6(b)). The ON/OFF ratios (read at 0.3 V) of the Pt/BTO/LNO, Pt/BTO/CCMO and Pt/BTO/LSMO devices are ~255, ~16 and ~10, respectively. These ON/OFF ratios are all below 1000, consistent with the ML predicted results (see Table 3).

Besides the different ON/OFF ratios, another interesting difference among these devices is also observed during the first half cycle of the voltage sweep. Specifically, the Pt/BTO/LNO and Pt/BTO/LSMO devices exhibits an initial LRS, which is switched to an HRS when the $0 \rightarrow 4$ V scan is first applied (Figs. S3(a) and S3(c)) but remains in the LRS when the $0 \rightarrow -4$ V scan is first applied (Figs. S3(d) and S3(f)). However, the Pt/BTO/CCMO device remains in the initial HRS when the $0 \rightarrow 4$ V scan is first applied but exhibits the resistance change when the $0 \rightarrow -4$ V scan is first applied (Figs. S3(b) and S3(e)). These results can be well correlated with the initial polarization directions in the three devices. In the Pt/BTO/LNO and Pt/BTO/LSMO (Pt/BTO/CCMO) device, the initial polarization direction is upward (downward) (Figs. 5(h)–5(j)), and hence the polarization switching and associated resistive switching occurs only when the $0 \rightarrow 4$ V ($0 \rightarrow -4$ V) scan is first applied. These results in turn suggest that the resistive switching is caused by the ferroelectric polarization reversal. *J*-*V* curve fittings were further performed, revealing that the resistive switching mechanism in these FTJs is the polarization modulation of tunnel barrier (see Fig. S4 and Table S4 for details).

Figure 6(c) shows the resistive switching behaviors of the Gra/BTO/LNO, Gra/BTO/CCMO and Gra/BTO/LSMO devices, with the stabilities of HRS and LRS demonstrated in Fig. 6(d). The SET transition occurs in the positive voltage regime for all the Gra-electroded devices, which is different from that observed in Pt-electroded devices (see comparison between Figs. 6(a) and 6(c)), the origin for which is explained in Fig. S4 and Table S4. Moreover, compared with their respective Pt-electroded counterparts, all the Gra-electroded devices exhibit larger hysteresis windows. The ON/OFF ratios (read at 0.3 V) of the Gra/BTO/LNO and Gra/BTO/CCMO devices are ~8540 and ~7890, respectively, which are well above 1000. However, the ON/OFF ratio of the Gra/BTO/LSMO device is ~113, still below 1000. These ON/OFF ratios (Fig. 6(e)) are well consistent with the ML predicted results (see Table 3). Note that the area and thickness of the Gra TE can have certain effects on the ON/OFF ratio, but they will not change the ON/OFF ratio significantly (see Fig. S5 for evidence).

Through the performance comparison among the above six FTJ devices, it is thus experimentally confirmed that FTJs with {Gra, CCMO} and {Gra, LNO} electrode pairs can achieve high ON/OFF ratios of ≥1000. Why the {Gra, CCMO} and {Gra, LNO} electrode pairs are favorable have been explained in Sec. 2.3 and the enhanced barrier height modulations with these electrode pairs are demonstrated in Table S4. However, using the Gra TE or the CCMO (or LNO) BE solely is not a sufficient condition for an ON/OFF ratio of ≥1000.

3. Conclusion

We have demonstrated an ML-based strategy capable of guiding the experimental development of high-performance FTJs. Various ML models were trained on a dataset containing 152 FTJ samples, among which the gradient boosting classification model achieved the highest prediction accuracy. Based on the feature importance ranking given by the gradient boosting model and the association

rule mining, it was extracted that the utilizations of {Gra, LNO} and {Gra, CCMO} electrode pairs were likely to result in high ON/OFF ratios in FTJs. By using these electrode pairs and applying the genetic algorithm to search other feature values, two previously unreported FTJs: Gra/BTO/LNO and Gra/BTO/CCMO were predicted to exhibit ON/OFF ratios higher than 1000. Guided by the ML predictions, the Gra/BTO/LNO and Gra/BTO/CCMO FTJs were experimentally fabricated. They exhibited ON/OFF ratios as high as ~8540 and ~7890, respectively, well consistent with the predicted results. Our study therefore demonstrates that ML is a particularly useful tool to guide the experimental development of FTJs with high ON/OFF ratios. It should be emphasized that ML can also be used to investigate other important performance metrics of FTJs, such as retention, endurance, speed, and energy consumption, given that sufficient data are available. Besides, the applications of ML can be extended to the development of other memory devices, such as resistive switching devices, phase change memories and magnetic tunnel junctions, which will stimulate great interest in the community of information materials and devices.

4. Experimental Section

Device Fabrication: Pulsed laser deposition (PLD) with KrF excimer laser ($\lambda = 248$ nm) was used for the film depositions. First, LNO (~30 nm), CCMO (~20 nm) and LSMO (~30 nm) BE layers were epitaxially grown on different STO (001) substrates at different temperatures of 600°C, 670 °C and 720 °C, respectively, and under the different oxygen pressures of 15 Pa, 10 Pa and 20 Pa, respectively. Then, ultrathin BTO films (~4.8 nm) were grown on the LNO, CCMO and LSMO BE layers at 700°C under an oxygen pressure of 1 Pa. Afterward, the deposited films were cooled to room temperature at a rate of 10°C/min in an oxygen atmosphere of 1000 Pa.

To construct the FTJs, Pt TEs (diameter: 16 μm) were fabricated on the BTO/LNO, BTO/CCMO and BTO/LSMO films by optical lithography followed by sputtering and lift-off. In addition, Gra top electrodes were fabricated on the three films by mechanical exfoliation using sticky tapes. After fabricating these TEs, six FTJs, i.e., Pt/BTO/LNO, Pt/BTO/CCMO, Pt/BTO/LSMO, Gra/BTO/LNO, Gra/BTO/CCMO and Gra/BTO/LSMO were constructed.

Structural and electrical characterizations: Crystalline phases of the films were investigated using the synchrotron XRD (Shanghai Synchrotron Radiation Facility). The X-ray wavelength was 0.687 Å. The microstructures were further studied using a Themis Z STEM (Thermo Fisher Scientific) operated at 200 kV. Cross-sectional TEM samples were prepared following a conventional procedure consisting of cutting, grinding, polishing and ion milling.

Atomic force microscopy (AFM) and PFM were performed on an integrated scanning probe microscope (Asylum Cypher) to characterize the surface morphology and ferroelectricity, respectively. In PFM, both images and hysteresis loops were acquired in the DART (dual a.c. resonance tracking) model with an AC driving voltage of 0.8 V. Room-temperature resistive switching characteristics of the six FTJs were measured with a source meter (Keithley 6430) and a home-made probe station.

Acknowledgments

The authors would like to thank the National Natural Science Foundation of China (Nos. 92163210, U1932125, 52172143, 12174347, 61874158 and 92164109), Science and Technology Program of GuangZhou (No. 2019050001) and Natural Science of Guangdong Province (No. 2020A1515010996).

References

[1]Y. Yang, M. Wu, X. Li, H. Hu, Z. Jiang, Z. Li, X. Hao, C. Zheng, X. Lou, S. J. Pennycook and Z. Wen, The role of ferroelectric polarization in resistive memory properties of metal/insulator/semiconductor tunnel junctions: A comparative study, *CS Appl. Mater. Interfaces* **12**, 32935 (2020).

[2]H. J. Mao, C. Song, L. R. Xiao, S. Gao, B. Cui, J. J. Peng, F. Lib and F. Pan, Unconventional resistive switching behavior in ferroelectric tunnel junctions, *Phys. Chem. Chem. Phys.* **17**, 10146 (2015).

[3]R. Berdan, T. Marukame, K. Ota, M. Yamaguchi, M. Saitoh, S. Fujii, J. Deguchi and Y. Nishi, Low-power linear computation using nonlinear ferroelectric tunnel junction memristors, *Nat. Electron.* **3**, 259 (2020).

[4]A. Chanthbouala, A. Crassous, V. Garcia, K. Bouzehouane, S. Fusil, X. Moya, J. Allibe, B. Dlubak, J. Grollier, S. Xavier, C. Deranlot, A. Moshar, R. Proksch, N. D. Mathur, M. Bibes and A. Barthelemy, Solid-state memories based on ferroelectric tunnel junctions, *Nat. Nanotechnol.* **7**, 101 (2012).

[5]S. Boyn, J. Grollier, G. Lecerf, B. Xu, N. Locatelli, S. Fusil, S. Girod, C. Carretero, K. Garcia, S. Xavier, J. Tomas, L. Bellaiche, M. Bibes, A. Barthelemy, S. Saighi and V. Garcia, Learning through ferroelectric domain dynamics in solid-state synapses, *Nat. Commun.* **8**, 14736 (2017).

[6]R. Guo, W. Lin, X. Yan, T. Venkatesan and J. Chen, Ferroic tunnel junctions and their application in neuromorphic networks, *Appl. Phys. Rev.* **7**, 011304 (2020).

[7]P. Hou, J. Wang and X. Zhong, Investigation of multilevel data storage in silicon-based polycrystalline ferroelectric tunnel junction, *Sci. Rep.* **7**, 4525 (2017).

[8]Z. Wen, C. Li, D. Wu, A. Li and N. Ming, Ferroelectric-field-effect-enhanced electroresistance in metal/ferroelectric/semiconductor tunnel junctions, *Nat. Mater.* **12**, 617 (2013).

[9]A. Sokolov, O. Bak, H. Lu, S. Li and E. Y. Tsymbal, A. Gruverman, Effect of epitaxial strain on tunneling electroresistance in ferroelectric tunnel junctions, *Nanotechnology* **26**, 305202 (2015).

[10]R. Guo, Y. Zhou, L. Wu, Z. Wang, Z. Lim, X. Yan, W. Lin, H. Wang, H. Y. Yoong, S. Chen, Ariando, T. Venkatesan, J. Wang, G. M. Chow, A. Gruverman, X. Miao, Y. Zhu and J. Chen, Control of synaptic plasticity learning of ferroelectric tunnel memristor by nanoscale interface engineering, *ACS Appl. Mater. Inter*face, **10**, 12862 (2018).

[11]C. Li, L. Huang, T. Li, W. Lu, X. Qiu, Z. Huang, Z. Liu, S. Zeng, R. Guo, Y. Zhao, K. Zeng, M. Coey, J. Chen, Ariando and T. Venkatesan, Ultrathin $BaTiO_3$-based ferroelectric tunnel junctions through interface engineering, *Nano. Lett.* **15**, 2568 (2015).

[12]W. Lu, C. Li, L. Zheng, J. Xiao, W. Lin, Q. Li, X. R. Wang, Z. Huang, S. Zeng, K. Han, W. Zhou, K. Zeng, J. Chen, Ariando, W. Cao and T. Venkatesan, Multi-nonvolatile state resistive switching arising from ferroelectricity and oxygen vacancy migration, *Adv. Mater.* **29**, 1606165 (2017).

[13]X. Wang, M. Wu, F. Wei, Y. Zhang, C. Zheng, X. Lou, S. J. Pennycook and Z. Wen, Electroresistance of Pt/$BaTiO_3$/$LaNiO_3$ ferroelectric tunnel junctions and its dependence on $BaTiO_3$ thickness, *Mater. Res. Exp.* **6**, 046307 (2019).

[14]L. Wang, M. R. Cho, Y. J. Shin, J. R. Kim, S. Das, J. -G. Yoon, J.-S. Chung and T. W. Noh, Overcoming the fundamental barrier thickness limits of ferroelectric tunnel junctions through $BaTiO_3$/$SrTiO_3$ composite barriers, *Nano Lett.* **16**, 3911 (2016).

[15]J. Li, N. Li, C. Ge, H. Huang, Y. Sun, P. Gao, M. He, C. Wang, G. Yang and K. Jin, Giant electroresistance in ferroionic tunnel junctions, *iScience* **16**, 368 (2019).

[16]K. J. Choi, M. Biegalski, Y. L. Li, A. Sharan, J. Schubert, R. Uecker, P. Reiche, Y. B. Chen, X. Q. Pan, V. Gopalan, L.-Q. Chen, D. G. Schlom and C. B. Eom, Enhancement of ferroelectricity in strained $BaTiO_3$ thin films, *Science* **306**, 1005 (2004).

[17]R. Soni, A. Petraru, P. Meuffels, O. Vavra, M. Ziegler, S. K. Kim, D. S. Jeong, N. A. Pertsev and H. Kohlstedt, Giant electrode effect on tunnelling electroresistance in ferroelectric tunnel junctions, *Nat. Commun.* **5**, 5414 (2014).

[18]D. Pantel and M. Alexe, Electroresistance effects in ferroelectric tunnel barriers, *Phys. Rev. B* **82**, 134105 (2010).

[19]Y. Goh and S. Jeon, The effect of the bottom electrode on ferroelectric tunnel junctions based on CMOS-compatible HfO_2, *Nanotechnology* **29**, 335201 (2018).

[20]V. Garcia, S. Fusil, K. Bouzehouane, S. Enouz-Vedrenne, N. D. Mathur, A. Barthelemy and M. Bibes, Giant tunnel electroresistance for non-destructive readout of ferroelectric states, *Nature* **460**, 81 (2009).

[21]S. Boyn, A. M. Douglas, C. Blouzon, P. Turner, A. Barthélémy, M. Bibes, S. Fusil, J. M. Gregg and V. Garcia, Tunnel electroresistance in $BiFeO_3$ junctions: Size does matter, *Appl. Phys. Lett.* **109**, 232902 (2016).

[22]K.M. Niang, G. Bai, H. Lu and J. Robertson, Microstructure scaling in metal-insulator-transitions of atomic layer deposited VO_2 films, *Solid State Electron*. **183**, 108046 (2021).

[23]P. Hou, J. Wang, X. Zhong and Y. Wu, A ferroelectric memristor based on the migration of oxygen vacancies, *RSC Adv.* **6**, 54113 (2016).

[24]S. Zhang, L. Zhang, L. Wang, F. Wang and G. Pan, A flexible e-skin based on micro-structured PZT thin films prepared via a low-temperature PLD method, *J. Mater. Chem. C* **7**, 4760 (2019).

[25]F. E. Bock, R. C. Aydin, C. J. Cyron, N. Huber, S. R. Kalidindi and B. Klusemann, A review of the application of machine learning and data mining approaches in continuum materials mechanics, *Front. Mater.* **6**, 110 (2019).

[26]P. V. Balachandran, B. Kowalski, A. Sehirlioglu and T. Lookman, Experimental search for high-temperature ferroelectric perovskites guided by two-step machine learning, *Nat. Commun.* **9**, 1668 (2018).

[27]R. Yuan, Z. Liu, P. V. Balachandran, D. Xue, Y. Zhou, X. Ding, J. Sun, D. Xue and T. Lookman, Accelerated discovery of large electrostrains in $BaTiO_3$-based piezoelectrics using active learning, *Adv. Mater.* **30**, 1702884 (2018).

[28]W. Sun, Y. Zheng, K. Yang, Q. Zhang, A. A. Shah, Z. Wu, Y. Sun, L. Feng, D. Chen, Z. Xiao, S. Lu, Y. Li and K. Sun, Machine learning-assisted molecular design and efficiency prediction for high-performance organic photovoltaic materials, *Sci. Adv.* **5**, 11 (2019).

[29]X. Yang, J. Xi, Y. Sun, Y. Zhang, G. Zhou and W.-Y. Wong, A dopant-free twisted organic small-molecule hole transport material for inverted planar perovskite solar cells with enhanced efficiency and operational stability, *Nano Energy* **64**, 103946 (2019).

[30]C. She, Q. Huang, C. Chen, Y. Jiang, Z. Fan and J. Gao, Machine learning-guided search for high-efficiency perovskite solar cells with doped electron transport layers, *J. Mater. Chem. A* **9**, 25168 (2021).

[31]Z. Xi, J. Ruan, C. Li, C. Zheng, Z. Wen, J. Dai, A. Li and D. Wu, Giant tunnelling electroresistance in metal/ferroelectric/semiconductor tunnel junctions by engineering the Schottky barrier, *Nat. Commun.* **8**, 15217 (2017).

[32]F. Ambriz-Vargas, G. Kolhatkar, R. Thomas, R. Nouar, A. Sarkissian, C. Gomez-Yáñez, M. A. Gauthier and A. Ruediger, Tunneling electroresistance effect in a Pt/$Hf_{0.5}Zr_{0.5}O_2$/Pt structure, *Appl. Phys. Lett.* **110**, 093106 (2017).

[33]H. Y. Yoong, H. Wang, J. Xiao, R. Guo, P. Yang, Y. Yang, S. T. Lim, J. Wang, T. Venkatesan and J. Chen, Tunneling electroresistance effect in ultrathin $BiFeO_3$-based ferroelectric tunneling junctions, *Appl. Phys. Lett.* **109**, 242901 (2016).

[34]C. L. Li, Z. H. Chen, Y. L. Zhou and D. F. Cui, Effect of oxygen content on the dielectric and ferroelectric properties of laser-deposited $BaTiO_3$ thin films, *J. Phys. Condens. Matter.* **13**, 5261 (2001).

[35]Q. Luo, Y. Cheng, J. Yang, R. Cao, H. Ma, Y. Yang, R. Huang, W. Wei, Y. Zheng, T. Gong, J. Yu, X. Xu, P. Yuan, X. Li, L. Tai, H. Yu, D. Shang, Q. Liu, B. Yu, Q. Ren, H. Lv and M. Liu, A highly CMOS compatible hafnia-based ferroelectric diode, *Nat. Commun*. **11**, 1 (2020).

[36]J. Zhu, W. B. Luo and Y. R. Li, Growth and properties of $BiFeO_3$ thin films deposited on $LaNiO_3$-buffered $SrTiO_3$ (0 0 1) and (1 1 1) substrates by PLD, *Appl. Surf. Sci.* **255**, 3466 (2008).

[37]C. Yoon, J. H. Lee, S. Lee, J. H. Jeon, J. T. Jang, D. H. Kim, Y. H. Kim and B. H. Park, Synaptic plasticity selectively activated by polarization-dependent energy-efficient ion migration in an ultrathin ferroelectric tunnel junction, *Nano. Lett.* **17**, 1949 (2017).

[38]F. Y. Bruno, S. Boyn, S. Fusil, S. Girod, C. Carrétéro, M. Marinova, A. Gloter, S. Xavier, C. Deranlot, M. Bibes, A. Barthélémy and V. Garcia, Millionfold resistance change in ferroelectric tunnel junctions based on nickelate electrodes, *Adv. Electron. Mater.* **2**, 1500245 (2016).

[39]M. Sokolova and G. Lapalme, A systematic analysis of performance measures for classification tasks, *Inf. Process. Manag.* **45**, 427 (2009).

[40]J. P. Velev, J. D. Burton, M. Y. Zhuravlev and E. Y. Tsymbal, Predictive modelling of ferroelectric tunnel junctions, *npj Comput. Mater*. **2**, 1 (2016).

[41]A. Gruverman, D. Wu, H. Lu, Y. Wang, H. W. Jang, C. M. Folkman, M. Ye. Zhuravlev, D. Felker, M. Rzchowski, C.-B. Eom and E. Y. Tsymbal, Tunneling electroresistance effect in ferroelectric tunnel junctions at the nanoscale, *Nano Lett.* **9**, 3539 (2009).

[42]H. K. Yoo, Y. J. Chang, L. Moreschini, H.-D. Kim, C. H. Sohn, S. Sinn, J. S. Oh, C.-T. Kuo, A. Bostwick, E. Rotenberg and T. W. Noh, Insulating-layer formation of metallic $LaNiO_3$ on Nb-doped $SrTiO_3$ substrate, *Appl. Phys. Lett.* **106**, 121601 (2015).

[43]H. Yamada, M. Marinova, P. Altuntas, A. Crassous, L. Begon-Lours, S. Fusil, E. Jacquet, V. Garcia, K. Bouzehouane, A. Gloter, J. E. Villegas, A. Barthelemy and M. Bibes, Ferroelectric control of a Mott insulator, *Sci. Rep.* **3**, 2834 (2013).

[44]S. Zhang, Spin-dependent surface screening in ferromagnets and magnetic tunnel junctions, *Phys. Rev. Lett*. **83**, 640 (1999).

[45]D. J. Kim, H. Lu, S. Ryu, C.-W. Bark, C. B. Eom, E. Y. Tsymbal and A. Gruverman, Ferroelectric tunnel memristor, *Nano Lett.* **12**, 5697 (2012).

[46]Ji. Wu, H.-Y. Chen, N. Yang, J. Cao, X. Yan, F. Liu, Q. Sun, X. Ling, J. Guo and H. Wang, High tunnelling electroresistance in a

ferroelectric van der Waals heterojunction via giant barrier height modulation, *Nat. Electron.* **3**, 466 (2020).
[47]M. J. Calderón and E. Bascones, Correlated states in magic angle twisted bilayer graphene under the optical conductivity scrutiny, *npj Quantum Mater.* **5**, 57 (2020).
[48]Y. Matsubara, K. S. Takahashi, Y. Tokura and M. Kawasaki, Single-crystalline $BaTiO_3$ films grown by gas-source molecular beam epitaxy, *Appl. Phys. Exp*. **7**, 125502 (2014).
[49]J. A. Cortés, J. Camargo, M. F. Rachia, F. Rubio-Marcos, L. Ramajo, M. Castro and M. A. Ramírez, Influence of the sintering temperature on ferroelectric properties of potassium-sodium niobate piezoelectric ceramics, *J. Adv. Dielectr*. **11**, 2140002 (2021).
[50]D. Lee, B. Chul Jeon, A. Yoon, Y. Jae Shin, M. H. Lee, T. K. Song, S. D. Bu, M. Kim, J. Chung, J.-G. Yoon and T. W. Noh, Flexoelectric control of defect formation in ferroelectric epitaxial thin films, *Adv. Mater.* **26**, 5005 (2014).
[51]Q. Huang, Z. Fan, J. Rao, T. Yang, X. Zhang, D. Chen, M. Qin, M. Zeng, X. Lu, G. Zhou, X. Gao and J.-M. Liu, Significant modulation of ferroelectric photovoltaic behavior by a giant macroscopic flexoelectric effect induced by strain-relaxed epitaxy, *Adv. Electron. Mater*. **8**, 2100612 (2022).
[52]F. Zhang, Q. Miao, G. Tian, Z. Lu, L. Zhao, H. Fan, X. Song, Z. Li, M. Zeng, X. Gao and J. Liu, Unique nano-domain structures in self-assembled $BiFeO_3$ and $Pb(Zr, Ti)O_3$ ferroelectric nanocapacitors, *Nanotechnology* **27**, 015703 (2015).
[53]W. Peng, J. Mun, Q. Xie, J. Chen, L. Wang, M. Kim and T. W. Noh, Oxygen vacancy-induced topological nanodomains in ultrathin ferroelectric films, *npj Quantum Mater.* **6**, 48 (2021).
[54]Y. Chu, Q. He, C. Yang, P. Yu, L. W. Martin, P. Shafer and R. Ramesh, Nanoscale control of domain architectures in $BiFeO_3$ thin films, *Nano Lett*. **9**, 1726 (2009).